

Light from the Hidden Sector

—

Experimental Signatures of Paraphotons

M. Ahlers¹, H. Gies², J. Jaeckel³, J. Redondo⁴ and A. Ringwald¹

¹*Deutsches Elektronen Synchrotron DESY,
Notkestrasse 85, D-22607 Hamburg, Germany*

²*Institute for Theoretical Physics, Heidelberg University,
Philosophenweg 16, D-69120 Heidelberg, Germany*

³*Centre for Particle Theory, Durham University,
Durham, DH1 3LE, United Kingdom*

⁴*Grup de Física Teòrica and Institut de Física d'Altes Energies
Universitat Autònoma de Barcelona, 08193 Bellaterra, Barcelona, Spain*

Abstract

Optical precision experiments are a powerful tool to explore hidden sectors of a variety of standard-model extensions with potentially tiny couplings to photons. An important example is given by extensions involving an extra light $U(1)$ gauge degree of freedom, so-called paraphotons, with gauge-kinetic mixing with the normal photon. These models naturally give rise to minicharged particles which can be searched for with optical experiments. In this paper, we study the effects of paraphotons in such experiments. We describe in detail the role of a magnetic field for photon-paraphoton oscillations in models with low-mass minicharged particles. In particular, we find that the upcoming light-shining-through-walls experiments are sensitive to paraphotons and can distinguish them from axion-like particles.

1 Introduction

Extensions beyond the current standard model of particle physics often involve a hidden sector, *i.e.*, an experimentally so far unobserved set of degrees of freedom very weakly coupled to standard-model particles. Whereas present and future accelerator experiments are generally devoted to the search for new heavy particles, the potential discovery of a new weakly coupled light particle requires high-precision experiments for which non-accelerator setups often appear most promising.

Optical experiments can provide for such a powerful laboratory tool, since optical photons can be manipulated and detected with a great precision. If a hypothetical hidden sector couples effectively to photons, optical experiments can have a significant discovery potential or, alternatively, can put stringent laboratory bounds on standard-model extensions, since both photon sources and detectors can be under full experimental control.

An example of such experiments are laser polarization experiments, such as BFRT [1], PVLAS [2], and Q&A [3], where linearly polarized laser light is sent through a transverse magnetic field, and changes in the polarization state are searched for. The real and virtual production of axion-like [4, 5] (ALP) or minicharged [6] (MCP) particles would lead to observable signals such as an apparent rotation and an ellipticity of the outgoing laser beam. Similar planned experiments in this direction are based also on high-intensity lasers [7].

Another powerful tool are so called light-shining-through-walls (LSW) experiments, such as BFRT [1, 8]. Here, laser light is shone onto a wall, and one searches for photons that appear behind the wall. Vacuum oscillations of photons into paraphotons with sub-eV masses would lead to a non-vanishing rate of photons behind the wall [9]. In the presence of a magnetic field, photons can oscillate into axion-like particles, which can then be reconverted into photons behind the wall by another magnetic field [10, 11, 12, 13].¹

Presently, there are several second generation LSW experiments worldwide, such as ALPS [17], BMV [18], GammeV [19], LIPSS [20], OSQAR [21], and PVLAS [22], under construction or serious consideration (for a review, see Refs. [23, 24]). These efforts are partially motivated by the report from the PVLAS collaboration of evidence for a non-zero apparent rotation of the polarization plane of a laser beam after passage through a magnetic field [2]. While the size of the observed effect greatly exceeds the expectations from quantum electrodynamics [25, 26, 27, 28], it is compatible with a photon-ALP oscillation hypothesis or with the production of light minicharged particles [29]. Although the couplings and masses required for an explanation of PVLAS seem to be in serious conflict with bounds coming from astrophysical considerations [30, 31], there are various ways to evade them [32, 33, 34, 35, 36, 37, 38, 39, 40, 41] (see, however, Ref. [42]). This makes it

¹Also, astrophysical observations of light rays from binary pulsar systems [14], dimming features in the spectra of TeV gamma sources [15], or regenerated photons from cosmic ALPs originating from the Crab pulsar [16] could be a useful optical probe.

extremely important to check these interpretations in laboratory experiments.

LSW experiments seem well-suited to distinguish between ALPs and minicharged particles. Only in the former case, we expect a sizeable rate of regenerated photons. However, natural models with minicharged particles also contain at least one paraphoton [43]. In this paper, we include the effects of paraphotons and discuss in detail how this can lead to a non-vanishing signal in LSW experiments that is nevertheless distinguishable from the one expected in the ALP case. Moreover, we show that the presence of the paraphoton significantly alters the signals in polarization experiments.

The paper is organized as follows. In Sect. 2, we briefly review how minicharges arise in models with paraphotons. In Sects. 3 and 4, we show how paraphotons can lead to a signal in LSW experiments. In Sect. 5, we discuss how the predictions for rotation and ellipticity measurements change in models with paraphotons. In realistic experiments, the magnetic field region has a finite spatial size. For small, but non-vanishing paraphoton mass, this can have significant effects, as we explain in Sect. 6. In Sect. 7, we give explicit examples in which signals of a paraphoton model are compared to those of a pure minicharged particle model without paraphoton. Furthermore, we use data from the BFRT experiment to illustrate the sensitivity of such optical setups. Finally, we summarize and conclude in Sect. 8.

2 Paraphotons and minicharged particles

Minicharged particles arise very naturally in models with extra $U(1)$ gauge degrees of freedom [9, 43]. In this section, we briefly review how kinetic mixing leads to minicharged particles and provide some details on models that have been proposed to explain the PVLAS result.

Let us begin with the simplest model with two $U(1)$ gauge groups, one being our electromagnetic $U(1)_{\text{QED}}$, the other a hidden-sector $U(1)_{\text{h}}$ under which all standard model particles have zero charge. The most general Lagrangian allowed by the symmetries is

$$\mathcal{L} = -\frac{1}{4}F^{\mu\nu}F_{\mu\nu} - \frac{1}{4}B^{\mu\nu}B_{\mu\nu} - \frac{1}{2}\chi F^{\mu\nu}B_{\mu\nu}, \quad (2.1)$$

where $F_{\mu\nu}$ is the field strength tensor for the ordinary electromagnetic $U(1)_{\text{QED}}$ gauge field A^μ , and $B^{\mu\nu}$ is the field strength for the hidden-sector $U(1)_{\text{h}}$ field B^μ , *i.e.*, the paraphoton. The first two terms are the standard kinetic terms for the photon and paraphoton fields, respectively. Because the field strength itself is gauge invariant for $U(1)$ gauge fields, the third term is also allowed by gauge and Lorentz symmetry. This term corresponds to a non-diagonal kinetic term, a so-called kinetic mixing.

From the viewpoint of a low-energy effective Lagrangian, χ is a completely arbitrary parameter. Embedding this into a more fundamental theory, it is plausible that $\chi = 0$

holds at a high-energy scale related to the fundamental theory. However, integrating out the quantum fluctuations below this scale generally tends to generate non-vanishing χ [43]. In a similar manner, kinetic mixing arises in many string theory models [35, 44, 45, 46, 47, 48, 49].

The kinetic term can be diagonalized by a shift

$$B^\mu \rightarrow \tilde{B}^\mu - \chi A^\mu. \quad (2.2)$$

Apart from a multiplicative renormalization of the gauge coupling, $e^2 \rightarrow e^2/(1 - \chi^2)$, the visible-sector fields remain unaffected by this shift.

Let us now assume that we have a hidden-sector fermion² h that has charge one under B^μ . Applying the shift (2.2) to the coupling term, we find:

$$e_h \bar{h} \not{B} h \rightarrow e_h \bar{h} \not{\tilde{B}} h - \chi e_h \bar{h} \not{A} h, \quad (2.3)$$

where e_h is the hidden-sector gauge coupling. We can read off that the hidden-sector particle now has a charge

$$\epsilon e = -\chi e_h \quad (2.4)$$

under the visible electromagnetic gauge field A^μ which has gauge coupling e . Since χ is an arbitrary number, the fractional electric charge ϵ of the hidden-sector fermion h is not necessarily integer.

For small $\chi \ll 1$, we observe that

$$|\epsilon| \ll 1, \quad (2.5)$$

and h becomes a minicharged particle. From now on we will concentrate on this case³.

So far we have considered the case of an unbroken $U(1)_h$ symmetry for the paraphoton. Let us now see what happens if we add a mass term,⁴

$$\mathcal{L}_\mu = \frac{1}{2} \mu^2 B^\mu B_\mu. \quad (2.6)$$

Applying the shift (2.2) results in a term

$$\mathcal{L}_\mu = \frac{1}{2} \mu^2 \left(\tilde{B}^\mu \tilde{B}_\mu - 2\chi \tilde{B}^\mu A_\mu + \chi^2 A^\mu A_\mu \right) \quad (2.7)$$

²Here and in the following, we will specialize to the case where the hidden-sector particle is a fermion. A generalization to scalars is straightforward and does not change the results qualitatively.

³Very small values of χ can be obtained in supersymmetric or string theories [44]. On the other hand, light particles with charge $\epsilon = \mathcal{O}(1)$ are excluded by several kinds of experiments [50, 31] and very massive particles give negligible contributions in experiments such as BFRT, PVLAS, Q&A or the upcoming optical experiments that will test the PVLAS particle interpretation.

⁴Adding a mass term is equivalent to breaking the paraphoton $U(1)_h$ via a Higgs mechanism and choosing unitary gauge.

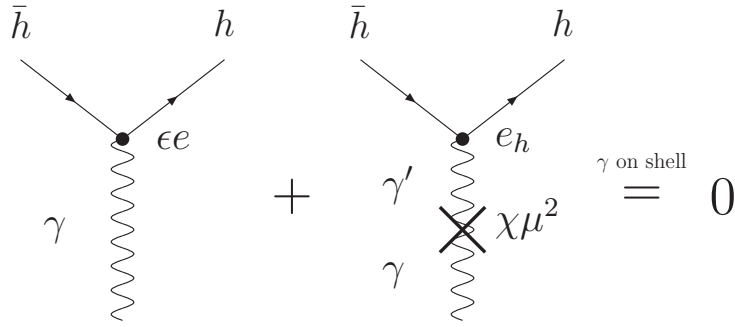


Figure 1: Two diagrams contributing to the coupling of the photon to the hidden-sector fermion h in a situation where the paraphoton is massive. The first is the direct contribution via the charge ϵe that arises from the shift (2.2) of the paraphoton field. The second is due to the non-diagonal mass term (2.7) and cancels the first diagram if the external photon is on shell and massless ($q^2 = 0$). Note that the second diagram is only present if the paraphoton has non-vanishing mass $\mu^2 \neq 0$.

that mixes photons with par photons.

To see how this affects the coupling of the hidden-sector fermion, let us write down the inverse propagator in our (A^μ, \tilde{B}^μ) basis,

$$P^{-1} = \begin{pmatrix} q^2 - \chi^2 \mu^2 & +\chi \mu^2 \\ +\chi \mu^2 & q^2 - \mu^2 \end{pmatrix}. \quad (2.8)$$

The effective charge of the hidden-sector fermion h is now obtained (to lowest order in χ) from

$$Q_{he} = \lim_{q^2 \rightarrow 0} q^2 P_{1j} C_j = -\epsilon e + \chi e_h = 0, \quad (2.9)$$

where

$$C = (-\epsilon e, e_h) \quad (2.10)$$

is the charge vector of h in the (A^μ, \tilde{B}^μ) basis. In this limit, the photon is put onto the mass shell, and the factor q^2 is included to cancel the trivial $1/q^2$ dependence of the Coulomb potential. The two contributions correspond to the two diagrams in Fig. 1. On shell, the minicharge is “undone” by the mass term. However, off shell or for massive photons (as, for instance, in a plasma), this is not the case.

Let us now move on to the slightly more involved case of the model presented in Ref. [34] (“MR model”). This model involves two par photons B_1^μ and B_2^μ . For clarity, we will in the following suppress Lorentz indices and use a matrix notation (A, B_1, B_2) , and similarly for the \tilde{B} . The Lagrangian for the gauge fields reads:

$$\mathcal{L} = -\frac{1}{4} F^T \mathcal{K} F + \frac{1}{2} A^T \mathcal{M} A, \quad (2.11)$$

with the kinetic mixing and mass matrix

$$\mathcal{K} = \begin{pmatrix} 1 & \chi & \chi \\ \chi & 0 & 0 \\ \chi & 0 & 0 \end{pmatrix}, \quad \mathcal{M} = \begin{pmatrix} 0 & 0 & 0 \\ 0 & \mu^2 & 0 \\ 0 & 0 & 0 \end{pmatrix}. \quad (2.12)$$

Again, we can diagonalize the kinetic term by shifting the fields,

$$\begin{aligned} B_1 &\rightarrow \tilde{B}_1 - \chi A, \\ B_2 &\rightarrow \tilde{B}_2 - \chi A. \end{aligned} \quad (2.13)$$

This leaves the ordinary electromagnetic gauge field unaffected (again up to a small renormalization).

The model of Ref. [34] has a hidden-sector fermion that lives in the bifundamental representation of the two paraphotons with charges $(0, 1, -1)$. Moreover, the two hidden gauge couplings are assumed to be equal $e_{h,1} = e_{h,2} \equiv e_h$. Applying (2.13), we find

$$e_h \bar{h} [B_1^\mu - B_2^\mu] \gamma_\mu h \rightarrow e_h \bar{h} [(\tilde{B}_1^\mu - \chi A^\mu) - (\tilde{B}_2^\mu - \chi A^\mu)] \gamma_\mu h = e_h \bar{h} [\tilde{B}_1^\mu - \tilde{B}_2^\mu] \gamma_\mu h. \quad (2.14)$$

For the moment, it seems as if the hidden-sector fermion has no interaction with the photon. However, we should not forget that one of the paraphotons is massive. In the new basis, the mass matrix reads

$$\tilde{\mathcal{M}} = \begin{pmatrix} \chi^2 \mu^2 & -\chi \mu^2 & 0 \\ -\chi \mu^2 & \mu^2 & 0 \\ 0 & 0 & 0 \end{pmatrix}. \quad (2.15)$$

As in the case of only one paraphoton, the mass term undoes the effects on the minicharges induced by the massive paraphoton (cf. Eq. (2.9)). Since the *second* paraphoton is massless, its contribution to the minicharge (cf. middle part of Eq. (2.14)) remains unaffected and the particle has an effective charge,

$$Q_h^{\text{MR}} e = +\chi e_h. \quad (2.16)$$

Finally, let us comment on situations where the virtuality of a process is high compared with the paraphoton mass scale, as, for instance, in the center of the sun. In this case, we cannot take the limit $q^2 \rightarrow 0$ in Eq. (2.9). Instead, we have to insert the virtuality of the process, implying that the minicharge is not undone by the mass term. At high virtuality, the small mass has basically no effect and the (first) paraphoton behaves more or less as if it were massless. For our case with two paraphotons, this means that the first paraphoton now contributes a charge $-e_h \chi$ to the effective electromagnetic coupling of h resulting in a total of

$$Q_h^{\text{MR}} \approx 0, \quad \text{for } q^2 \gg \mu^2. \quad (2.17)$$

In other words, the mass matrix (2.15) can be neglected, and we effectively have the case of two massless paraphotons and an interaction as in Eq. (2.14).

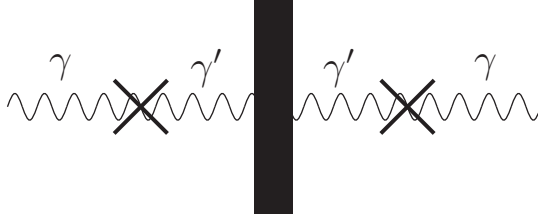


Figure 2: Schematic picture of a “Light-shining-through-walls” experiment in absence of a magnetic field. The crosses denote the non-diagonal mass terms that convert photons into paraxphotons. The photon γ oscillates into the paraxphoton γ' and, after the wall, back into the photon γ which can then be detected.

3 Light shining through walls I: $B=0$

In the previous section, we have seen how a non-diagonal mass matrix contributes to the effective charge of the hidden-sector fermion via a diagram that changes the photon into a paraxphoton (the second diagram of Fig. 1). This non-trivial propagation of the photon can have interesting effects in itself. Since the paraxphotons \tilde{B} do not interact with ordinary matter they can easily pass through a wall [9], giving rise to a process sketched in Fig. 2. There, we see how a photon is converted into a paraxphoton by the non-diagonal mass term. Subsequently, the paraxphoton passes through the wall and is then reconverted into an ordinary photon that can be detected.

The photon conversion into (massive) paraxphotons and back into photons very much resembles neutrino oscillations. Similarly to neutrinos, the interaction eigenstates are not equal to the propagation eigenstates.

In order to calculate the probability for an initial photon interaction eigenstate to propagate through a wall via this process, we start with the equations of motion in our tilde basis,

$$[\omega^2 \mathbf{1} + \partial_z^2 \mathbf{1} - \tilde{\mathcal{M}}] \begin{pmatrix} A \\ \tilde{B} \end{pmatrix} = \left[(\omega^2 + \partial_z^2) \begin{pmatrix} 1 & 0 \\ 0 & 1 \end{pmatrix} - \mu^2 \begin{pmatrix} \chi^2 & -\chi \\ -\chi & 1 \end{pmatrix} \right] \begin{pmatrix} A \\ \tilde{B} \end{pmatrix} = 0. \quad (3.1)$$

Here, we have suppressed the Lorentz structure. Both transverse polarization directions have to fulfill the same equation. In the second part, we have specialized to the case of only one massive paraxphoton. Note that this case is completely equivalent to the case with two paraxphotons in the model of Ref. [34], because the mass matrix (2.15) is non-vanishing only in the first two components and therefore the second paraxphoton does not mix with the photon (we will see in next section that this situation changes when photons propagate in an external magnetic field).

Experiment	Laser	Cavity	Magnets
ALPS	532 nm; 200 Watt	–	$B_1 = B_2 = 5$ T $\ell_1 = \ell_2 = 4.21$ m
BFRT	~ 500 nm; 3 Watt	$N_{\text{pass}} = 200$	$B_1 = B_2 = 3.7$ T $\ell_1 = \ell_2 = 4.4$ m
BMV	8×10^{21} γ per pulse	–	$B_1 = B_2 = 11$ T $\ell_1 = \ell_2 = 0.25$ m
GammeV	532 nm; 3.2 Watt	–	$B_1 = B_2 = 5$ T $\ell_1 = \ell_2 = 3$ m
LIPSS	900 nm; 3000 Watt	–	$B_1 = B_2 = 1.7$ T $\ell_1 = \ell_2 = 1$ m
OSQAR	1064 nm; 1000 Watt	$N_{\text{pass}} \sim 10000$	$B_1 = B_2 = 9.5$ T $\ell_1 = \ell_2 = 7$ m
PVLAS	1064 nm; 0.02 Watt	$N_{\text{pass}} = 44000$	$B_1 = 5$ T, $\ell_1 = 1$ m $B_2 = 2.2$ T, $\ell_2 = 0.5$ m

Table 1: The benchmark values of “light-shining-through-walls” (LSW) experiments (for some of these experiments, the setup is still preliminary).

From Eq. (3.1), we find two propagating eigenstates,

$$\begin{aligned}
V_1(z, t) &= \begin{pmatrix} 1 \\ \chi \end{pmatrix} \exp(-i(\omega t \pm k_1 z)), \quad \text{with } k_1^2 = \omega^2, \\
V_2(z, t) &= \begin{pmatrix} -\chi \\ 1 \end{pmatrix} \exp(-i(\omega t \pm k_2 z)), \quad \text{with } k_2^2 = \omega^2 - \mu^2 + \mathcal{O}(\chi^2).
\end{aligned} \tag{3.2}$$

Let us now start with an initial state at $z = 0$ that is purely photonic⁵,

$$A(0, 0) = A_0 \begin{pmatrix} 1 \\ 0 \end{pmatrix} = A_0 \left(\frac{1}{1 + \chi^2} V_1(0, 0) - \frac{\chi}{1 + \chi^2} V_2(0, 0) \right). \tag{3.3}$$

The survival probability for an initial photon is

$$P_{\gamma \rightarrow \gamma}(z) = \frac{|A_1(z, t)|^2}{|A_0|^2} = 1 - 4\chi^2 \sin^2 \left(\frac{\Delta k z}{2} \right) + \mathcal{O}(\chi^4), \tag{3.4}$$

where

$$\Delta k = k_1 - k_2 \approx \frac{\mu^2}{2\omega}, \quad \text{for } \mu \ll \omega. \tag{3.5}$$

The conversion probability into paraxial photons is then obtained as [9]

$$P_{\gamma \rightarrow \gamma'}(z) = \frac{|A_2(z, t)|^2}{|A_0|^2} = 1 - \frac{|A_1(z, t)|^2}{|A_0|^2} = 4\chi^2 \sin^2 \left(\frac{\mu^2}{4\omega} z \right). \tag{3.6}$$

⁵In Appendix B, we argue that this is a reasonable choice for the initial state.

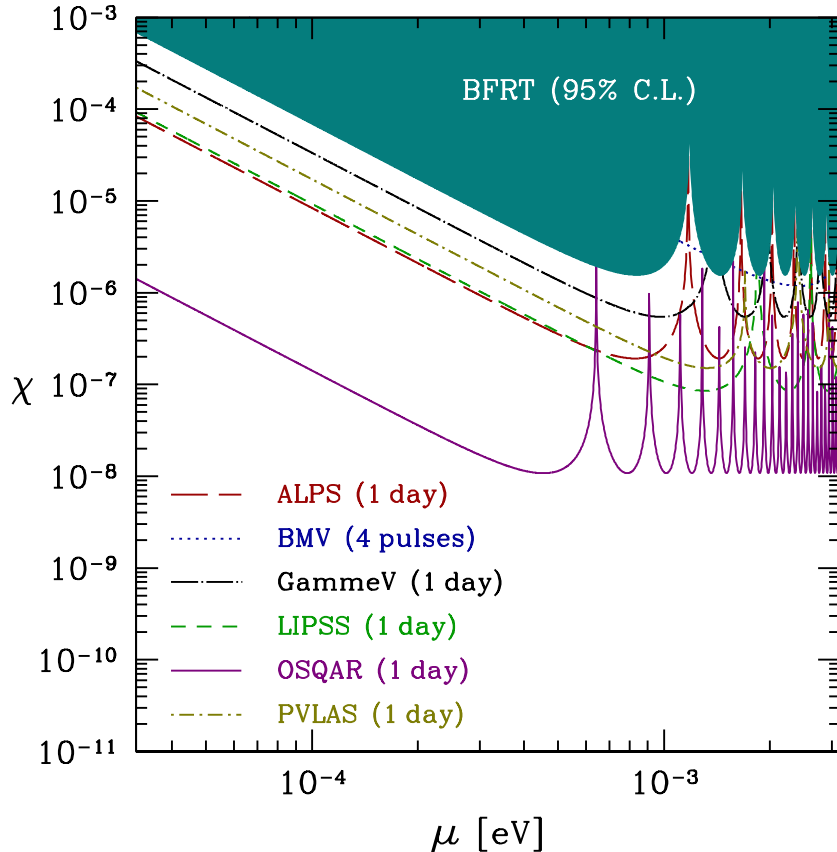


Figure 3: Projected sensitivity (one expected event per indicated time; no background; $\eta = 1$) of future LSW experiments to photon-paraphoton oscillations in the absence of a magnetic field. The shaded region shows the 95% exclusion region of BFRT.

In a light-shining-through-walls experiment as depicted in Fig. 2, with lengths ℓ_1 and ℓ_2 before and after the wall, the photon probability for a transit “through the wall” is then simply given by

$$P_{\text{trans}} = P_{\gamma \rightarrow \gamma'}(\ell_1) P_{\gamma' \rightarrow \gamma}(\ell_2) = 16\chi^4 \left[\sin\left(\frac{\ell_1 \mu^2}{4\omega}\right) \sin\left(\frac{\ell_2 \mu^2}{4\omega}\right) \right]^2. \quad (3.7)$$

Typically, the conversion probability $P_{\gamma \rightarrow \gamma'}(\ell_1)$ is enhanced by using a pair of facing mirrors before the wall. If the photon beam is reflected N_{pass} times, it will make $(N_{\text{pass}} + 1)/2$ “attempts” to cross the wall, enhancing the transmission probability by this same factor. The expected rate of observed photons in addition involves the total initial photon rate N_0 and the detection efficiency $\eta < 1$,

$$N = \eta N_0 \left[\frac{N_{\text{pass}} + 1}{2} \right] P_{\text{trans}}. \quad (3.8)$$

Figure 3 shows the limit from the BFRT experiment [1] and the projected sensitivity of the on-going experiments listed in Table 1, corresponding to one regenerated photon after

one day of observation. For $\mu \gtrsim 10^{-4}$ eV, this limit on the mixing parameter is better than the one from Cavendish-type laboratory searches for a fifth force [51, 52, 53].

4 Light shining through walls II: $B \neq 0$

In a classic light-shining-through-walls experiment [11, 12, 13], the light is shone through a transverse magnetic field. This is because these experiments typically look for axions [54, 55], whose production by virtue of their coupling to two photons requires a transverse magnetic field [10]. Therefore, let us study what happens in our photon-paraphoton system with a minicharged particle if we switch on such a magnetic field.

In a pure minicharged particle model without paraphotons, the conversion of photons into minicharged particles in a magnetic field does not produce a photon signal in the detector behind the wall. The particle-antiparticle pairs that are created from the photons [6] move away from each other under the influence of the magnetic field because they have opposite charges. Moreover, they typically have opposite momenta along the direction of the magnetic field lines separating them even further. In general, the particles will not annihilate again behind the wall and cannot be reconverted into photons⁶.

What is different if we include paraphotons? The *big* difference is that now photons can convert into paraphotons which then will pass through the wall. In the presence of a magnetic field, this coherent conversion is possible even for massless paraphotons. The relevant diagram for this transition is depicted in Fig. 4(b).

For a quantitative analysis, we again start from the equations of motion. We begin with the simple case of only one massless paraphoton. Without paraphotons, Fig. 4(a) would induce a non-vanishing refractive index. The photon would then satisfy the following equation of motion,

$$[(1 + 2\epsilon^2 e^2 \Delta N_i) \omega^2 - k^2] A_i = 0 \quad (\text{without paraphotons}). \quad (4.1)$$

The index i represents the two polarizations \parallel and \perp with respect to the magnetic field and $\epsilon^2 e^2 \Delta N_i = n_i - 1$ is the contribution to the refractive index of the photon caused by the diagram 4(a). The explicit expression for $\Delta N_i(\epsilon e \mathbf{B}, m_f)$ for a particle h with mass m_e is given in Appendix A. Various representations of ΔN_i and plots of the parameter dependencies can, for instance, be found in [57, 58, 59].

It is now straightforward to derive the contribution from Fig. 4(b) to our photon-

⁶In the present work, we assume that the wall thickness is bigger than the Compton wavelength of the minicharged particles. In this limit, we expect that the potential process of a photon propagating through the wall as a virtual minicharged particle pair is exponentially suppressed. The opposite limit requires a careful field-theoretical study of the photon polarization tensor near the wall, which is beyond the scope of the present work.

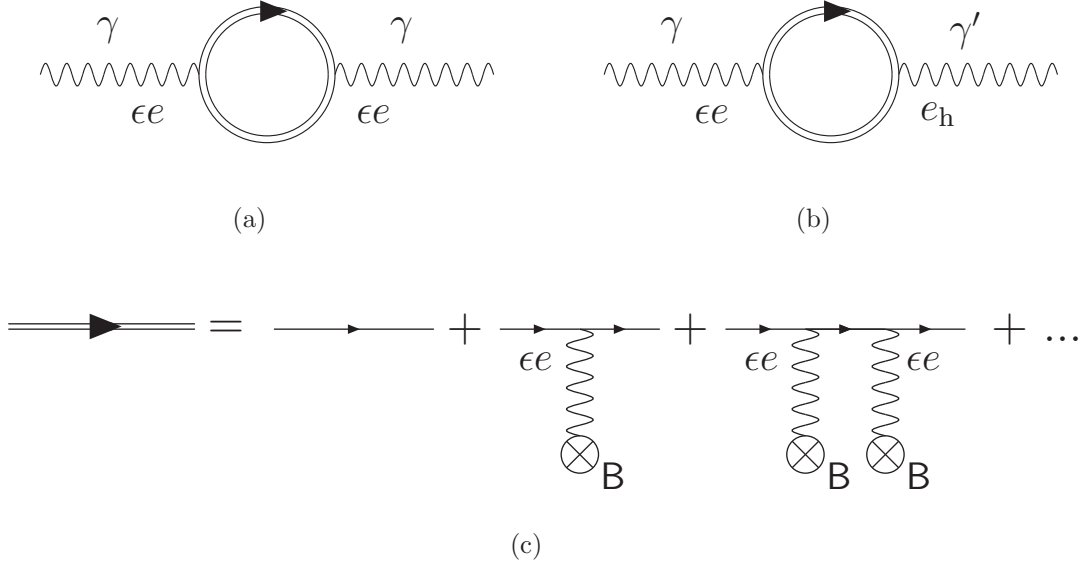


Figure 4: The contribution of minicharged particles to the polarization tensor 4(a). The real part leads to birefringence, whereas the imaginary part reflects the absorption of photons caused by the production of particle-antiparticle pairs. The analogous diagram 4(b) shows how minicharged particles mediate transitions between photons and paraphotons. Note that the latter diagram is enhanced with respect to the first one by a factor $\sim e_h/(\epsilon e) = 1/\chi$. The double line represents the complete propagator of the minicharged particle in an external magnetic field B as displayed in 4(c) [56].

paraphoton system. The full equation of motion becomes

$$\left[(1 + 2\epsilon^2 e^2 \Delta N_i) \omega^2 - k^2 \right] A_i + 2(\epsilon e) e_h \Delta N_i \omega^2 \tilde{B}_i = 0. \quad (4.2)$$

Equation (4.2) is not a closed equation for the photon, because it contains the paraphoton field. The equation of motion for the paraphoton can be obtained in complete analogy. We simply have to replace the two external photon legs in Fig. 4(a) with paraphotons and exchange the photon and the paraphoton field in Fig. 4(b),

$$\left[(1 + 2e_h^2 \Delta N_i) \omega^2 - k^2 \right] \tilde{B}_i + 2(\epsilon e) e_h \Delta N_i \omega^2 A_i = 0. \quad (4.3)$$

Using (2.4) to eliminate ϵ , we can write the complete set of equations as

$$\left[(\omega^2 + \partial_z^2) \begin{pmatrix} 1 & 0 \\ 0 & 1 \end{pmatrix} + 2\omega^2 e_h^2 \Delta N_i \begin{pmatrix} +\chi^2 & -\chi \\ -\chi & +1 \end{pmatrix} \right] \begin{pmatrix} A_i \\ \tilde{B}_i \end{pmatrix} = 0, \quad (4.4)$$

for one massless paraphoton.

This equation is completely equivalent to (3.1) if we replace

$$\mu^2 \rightarrow -2\omega^2 e_h^2 \Delta N_i. \quad (4.5)$$

The propagation eigenstates are already given in Eq. (3.2). There is only one slight complication that has to be dealt with when calculating the transition probability: ΔN_i is generally complex,

$$\Delta N_i = \Delta n_i + \frac{1}{2\omega} i\kappa_i. \quad (4.6)$$

Up to coupling factors corresponding to the external (para-)photon lines, Δn_i is the deviation of the real refractive index from 1, and κ_i denotes the absorption coefficient. Accounting for this, the transition probability is

$$P_{\gamma \rightarrow \gamma'}(z) = \chi^2 [1 + \exp(-e_h^2 \kappa_i z) - 2 \exp(-e_h^2 \kappa_i z / 2) \cos(e_h^2 \Delta n_i \omega z)]. \quad (4.7)$$

The total probability for a light-shining-through-walls experiment then is

$$P_{\text{trans}} = \left[\frac{N_{\text{pass}} + 1}{2} \right] \chi^4 [1 + \exp(-e_h^2 \kappa_i z) - 2 \exp(-e_h^2 \kappa_i z / 2) \cos(e_h^2 \Delta n_i \omega z)]^2. \quad (4.8)$$

Note the following features:

- The size of the photon-paraphoton mixing is controlled by χ^2 , but
- the typical oscillation length for the photon-paraphoton system is given by $1/(\omega e_h^2 \Delta n)$. The latter is by a factor χ^2 shorter than the typical length which might naively be expected from Fig. 4(a).
- The oscillations die out for non-vanishing κ_i and we get a non-oscillatory signal for experiments with a sufficiently long conversion region. This is rather useful, because the oscillations typically lead to “holes” in the sensitivity of the experiment for a given fixed experimental signal.
- The ΔN_i are non-vanishing for both polarization directions \parallel and \perp and we expect a signal for both polarizations. This might resemble a case in which light-shining-through-walls proceeds through an axion-like particle (ALP) with mixed parity interactions to photons⁷, as considered in Ref. [60]. However, for the most likely scenarios where the ALP has a definite parity, either pseudoscalar or scalar, a signal would be expected only for the \parallel or \perp mode.
- For practical purposes, it is useful that the oscillation length of the photon-paraphoton system is controllable by the external magnetic field (Δn and κ depend on \mathbf{B}). Varying the magnetic field, one can try to maximize the term in square brackets in Eqs. (4.7) or (4.8). For instance, the transition probability (4.7) asymptotically approaches χ^2 ; but for a suitable set of parameters such that $\kappa_i z \rightarrow 0$ and $\Delta n_i \omega z \rightarrow$

⁷Even in this case it can be easy to distinguish between a general ALP and paraphoton scenarios. In the second case, the ratio of the regeneration rates of the two polarization modes does depend on the photon energy and on the strength of the magnetic field, whereas this ratio is a constant for the former case.

π , the transition probability can increase up to $16\chi^2$. This is in contrast to the case of an ALP, where the oscillation length is completely determined by the mass of the ALP, which cannot be changed, and the frequency of the laser, which is at least more difficult to change.

At first glance, the insertion of a mass term seems straightforward on the basis of the equations of motion. However, as discussed in Sect. 2, we have to take into account that the effective h -photon coupling receives an additional contribution from the non-diagonal propagator, such that $Q_h = 0$. Therefore, ΔN_i vanishes in this case, and we get the same result as for $\mathbf{B} = 0$. Note that this simple argument implicitly assumes that the magnetic field is homogeneous and thus has infinite spatial extent, also transversally to the photon beam direction. The effects of a magnetic field with finite size will be discussed in Sect. 6.

Finally, let us turn to the full model [34] with two paraxial photons, one massless and one massive. As discussed in Sect. 2, the effective coupling of the particle h with charges $(0, 1, -1)$ to photons is $Q_h e = \chi e_h$, cf. Eq. (2.16). This determines ΔN as given in Section 6 and Appendix A. Taking the negative charge of h with respect to the second paraxial photon into account, the equation of motion reads

$$\left[(\omega^2 + \partial_z^2) \begin{pmatrix} 1 & 0 & 0 \\ 0 & 1 & 0 \\ 0 & 0 & 1 \end{pmatrix} - \mu^2 \begin{pmatrix} \chi^2 & -\chi & 0 \\ -\chi & 1 & 0 \\ 0 & 0 & 0 \end{pmatrix} + 2\omega^2 e_h^2 \Delta N_i \begin{pmatrix} 0 & 0 & 0 \\ 0 & 1 & -1 \\ 0 & -1 & 1 \end{pmatrix} \right] \begin{pmatrix} A_i \\ \tilde{B}_{1,i} \\ \tilde{B}_{2,i} \end{pmatrix} = 0. \quad (4.9)$$

The explicit regeneration probabilities are given in Appendix C. A quantitative discussion follows below in Sect. 7.

5 Dichroism and birefringence in models with paraxial photons

In the preceding sections, we have concentrated on light-shining-through-walls experiments. But imprints of paraxial photons can also be found in experiments that measure the change in the optical properties after propagation through the apparatus, as is, for instance, done in the BFRT, PVLAS and Q&A experiments.

Both rotation and ellipticity can be inferred from the photon-photon amplitude,

$$A_{\gamma \rightarrow \gamma}^i = \frac{A_1^i(z, t)}{A_0 \exp(i(kz - \omega t))}, \quad (5.1)$$

for different polarization directions i .

As we have already seen in Sect. 3, Eq. (3.4),

$$P_{\gamma \rightarrow \gamma}^i = |A_{\gamma \rightarrow \gamma}^i|^2 \quad (5.2)$$

is the survival probability for an incoming photon. In other words, $1 - |A_{\gamma \rightarrow \gamma}^i|$ is the decrease in amplitude for the different polarization directions. From this, we can easily find the rotation of an initially linear polarized beam entering at an angle θ ,

$$\Delta\theta = \frac{1}{2}(|A_{\gamma \rightarrow \gamma}^\perp| - |A_{\gamma \rightarrow \gamma}^\parallel|) \sin(2\theta) \approx \frac{1}{2} \text{Re}(A_{\gamma \rightarrow \gamma}^\perp - A_{\gamma \rightarrow \gamma}^\parallel) \sin(2\theta), \quad (5.3)$$

where the approximation is valid for amplitudes that are close to 1.

Phase shifts compared to an unmodified photon beam appear as the argument of the amplitude, $\text{Arg}(A_{\gamma \rightarrow \gamma}^{\perp, \parallel})$. One finds for the ellipticity,

$$\psi = \frac{1}{2}[\text{Arg}(A_{\gamma \rightarrow \gamma}^\parallel) - \text{Arg}(A_{\gamma \rightarrow \gamma}^\perp)] \sin(2\theta) \approx \frac{1}{2} \text{Im}(A_{\gamma \rightarrow \gamma}^\parallel - A_{\gamma \rightarrow \gamma}^\perp) \sin(2\theta). \quad (5.4)$$

As expected, neither rotation nor ellipticity appears in the absence of a magnetic field, because the amplitudes $A_{\gamma \rightarrow \gamma}^{\perp, \parallel}$ are equal. This is, of course, due to the fact that a simple Lorentz invariant mass term distinguishes no preferred direction.

In the presence of a magnetic field, however, the amplitudes differ, because the oscillation and absorption lengths are different for photons parallel \parallel and perpendicular \perp to the magnetic field.

Using the propagation eigenstates derived in Sects. 3 and 4, namely Eqs. (3.2), (3.5) and (4.5), we find the amplitude

$$A_{\gamma \rightarrow \gamma}^{\perp, \parallel} = 1 - \chi^2(1 - \exp(-i\Delta k^{\perp, \parallel} z - K^{\perp, \parallel} z)), \quad \text{for } \chi \ll 1, \quad (5.5)$$

where

$$\Delta k^{\perp, \parallel} = -\omega e_h^2 \Delta n^{\perp, \parallel}, \quad K^{\perp, \parallel} = \frac{1}{2} e_h^2 k^{\perp, \parallel}. \quad (5.6)$$

Inserting this into Eq. (5.3), we find:

$$\begin{aligned} \Delta\theta &= \frac{1}{2} \chi^2 [\cos(\Delta k^\perp z) \exp(-K^\perp z) - \cos(\Delta k^\parallel z) \exp(-K^\parallel z)] \sin(2\theta) \\ &\approx \left[\frac{1}{4} \epsilon^2 e^2 (\kappa^\parallel - \kappa^\perp) z + \frac{1}{4} \chi^2 \omega^2 [(e_h^2 \Delta n^\parallel)^2 - (e_h^2 \Delta n^\perp)^2] z^2 \right] \sin(2\theta), \quad \text{for } \Delta k z, K z \ll 1. \end{aligned} \quad (5.7)$$

The first term in the last line is the standard result for the rotation in a model without paraxial photons (cf. *e.g.* Ref. [29]). However, note that with paraxial photons where $\epsilon^2 e^2 = \chi^2 e_h^2$ this result holds only if the length z is much smaller than the oscillation length $1/(\omega e_h^2 \Delta n)$; the latter is by a factor χ^2 smaller than the naive expectation from the case without paraxial photons $1/(\omega \epsilon^2 e^2 \Delta n)$.

Similarly the ellipticity can be inferred from Eq. (5.4),

$$\begin{aligned} \psi &= -\frac{1}{2}\chi^2 [\sin(\Delta k^\parallel z) \exp(-K^\parallel z) - \sin(\Delta k^\perp z) \exp(-K^\perp z)] \sin(2\theta) \\ &\approx \frac{1}{2}\omega\epsilon_h^2 e^2 (\Delta n^\parallel - \Delta n^\perp) z \sin(2\theta), \quad \text{for } \Delta k z, K z \ll 1. \end{aligned} \quad (5.8)$$

Eqs. (5.3) and (5.4) are valid also for models with two paraxial photons. The determination of the rotation and ellipticity boils down to solving the equation of motion (4.9) and inserting into (5.1), (5.3) and (5.4). (The necessary expressions for the amplitudes can be found in Appendix C.) A quantitative discussion follows in Sect. 7.

6 Effects of a magnetic field with finite extent transverse to the photon beam

In Sect. 2, we have seen that, for massive paraxial photons, the ϵ electric charge resulting from the shift in the paraxial photon field is effectively canceled by the mass term as depicted in Fig. 1. However, this is true only if the photon coupling to the hidden-sector particle has $q^2 = 0$, *i.e.*, if it is on shell.

In realistic situations, the magnetic background field has a finite extent and the photons which build it up have a non-vanishing virtuality. In order to take this into account, we have to resum the diagrams in Fig. 1 also at non-vanishing virtuality. Resumming tree-level diagrams is equivalent to solving the equations of motion (this automatically includes also the higher-order diagrams with multiple mass insertions that were neglected in Fig. 1). Therefore, we have to solve the combined equations of motion for photon and paraxial photon – including the mass term – not only for the photons of the laser but also for the background magnetic field. To lowest order, we can neglect the index of refraction ΔN and we have (Lorentz structure suppressed),

$$[\nabla^2 \mathbf{1} - \tilde{\mathcal{M}}] \begin{pmatrix} A \\ \tilde{B} \end{pmatrix} = \left[\nabla^2 \begin{pmatrix} 1 & 0 \\ 0 & 1 \end{pmatrix} - \mu^2 \begin{pmatrix} \chi^2 & -\chi \\ -\chi & 1 \end{pmatrix} \right] \begin{pmatrix} A \\ \tilde{B} \end{pmatrix} = 0, \quad (6.1)$$

for a static background field.

To get an impression of the general behavior, we can solve (6.1) for a spherically symmetric situation with a point source. Similar to the two eigenmodes in Sect. 3, we find two solutions corresponding to a pure massless Coulomb-type potential and a massive

Yukawa-type potential⁸,

$$\begin{aligned}\phi_1(r) &= \begin{pmatrix} 1 \\ \chi \end{pmatrix} \frac{1}{r}, \\ \phi_2(r) &= \begin{pmatrix} -\chi \\ 1 \end{pmatrix} \frac{\exp(-\mu r)}{r}.\end{aligned}\tag{6.2}$$

For a source made up of ordinary matter, the potentials have to behave like $\sim (1, 0)^T 1/r$ for $r \rightarrow 0$ and the potential for matter fields takes the form,

$$\phi_{\text{matter}} \sim \frac{1}{1 + \chi^2} \frac{1}{r} \begin{pmatrix} 1 + \chi^2 \exp(-\mu r) \\ \chi(1 - \exp(-\mu r)) \end{pmatrix}.\tag{6.3}$$

A hidden-sector particle with charge vector $(\epsilon e, e_h)^T$ therefore sees an effective potential,

$$(\epsilon e, e_h)\phi_{\text{matter}} \sim \frac{1}{r} [\epsilon e + \chi e_h (1 - \exp(-\mu r))] + \mathcal{O}(\chi^2) = \frac{1}{r} \epsilon e \exp(-\mu r),\tag{6.4}$$

where we have used Eq. (2.4), $\epsilon e = -e_h \chi$, for the last equality. Note that this can be written as

$$(\epsilon e, e_h)\phi_{\text{matter}} \sim (\epsilon e, e_h)\phi_{\text{matter}}|_{\mu=0} \exp(-\mu r),\tag{6.5}$$

and therefore, these effects can be accounted for by using an effective magnetic field $\mathbf{B}_{\text{eff}}(r)$ in the calculation of ΔN , given by

$$\mathbf{B}_{\text{eff}}(r) = \mathbf{B}(1 + \mu r) \exp(-\mu r)\tag{6.6}$$

where \mathbf{B} is the standard magnetic field, calculated as if there were no paraphotons.

If the source is not pointlike we therefore expect a behavior,

$$\mathbf{B}_{\text{eff}}(r) \sim \begin{cases} \mathbf{B} \exp(-\mu r) & \text{for } \mu r \gg 1 \\ \mathbf{B} & \text{for } \mu r \ll 1 \end{cases},\tag{6.7}$$

where r is now a typical distance from the source.

For large distances, $r \gg 1/\mu$, we recover the result that the effective charge vanishes. But for smaller distances, residual effects of the epsilon charge remain. In typical experiments, the transverse size⁹ of the magnetic field is of the order of 10 cm. Remembering that $1 \text{ cm} \approx 1/(2 \times 10^{-5} \text{ eV})$ this can indeed become an important effect for paraphoton masses of the order of μeV .

A similar calculation can be done for the case of two paraphotons. In this case, the hidden-sector field is not directly coupled to the electromagnetic field (cf. Eq. (2.14)).

⁸In our simplified notation without any Lorentz structure, the potentials can be either the electric potential or the vector potential leading to magnetic fields, depending on whether the source is a charge or a current.

⁹The important length scale is the distance from the sources, *i.e.*, the currents.

The effective epsilon charge arises, because one paraphoton is massive and the other is massless, and the cancellation analogous to Fig. 1 is not complete. Therefore, we are not too surprised by the result,

$$\mathbf{B}_{\text{eff}}^{\text{MR}}(r) = \mathbf{B}(1 - (1 + \mu r) \exp(-\mu r)). \quad (6.8)$$

For extended sources, we then expect

$$\mathbf{B}_{\text{eff}}^{\text{MR}}(r) \sim \begin{cases} \mathbf{B} & \text{for } \mu r \gg 1 \\ \mathbf{B}(0 + \mathcal{O}(\mu r)) & \text{for } \mu r \ll 1 \end{cases}, \quad (6.9)$$

where r is again a typical distance from the source.

At large $r \gg 1/\mu$, this indeed looks like a particle with an effective charge ϵe . At small distances the charge is reduced. This effect is exactly the same as the one that is used to “switch off” the electric charge of the hidden-sector particle in astrophysical plasmas in order to avoid the astrophysical bounds on minicharged particles [34].

7 Quantitative analysis

The contribution of minicharged particles to the rotation and ellipticity in a pure MCP model has been studied in Refs. [6, 29]. If the minicharge originates from kinetic mixing, the presence of the paraphoton may lead to significant changes to these signals and will also contribute to LSW experiments. In this section, we give some explicit examples for the influence of the paraphoton.

Qualitatively, the most obvious difference is the possibility to have a non-vanishing LSW signal, which is hardly possible without paraphotons, since the MCPs are unlikely to recombine behind the wall and produce a photon. The upper panels of Fig. 5 show the transition probability of photons in a LSW experiment as a function of the experimental parameters B and ℓ , the strength and length of the magnetic field, respectively. Note, that we have non-vanishing transition probabilities for photons polarized parallelly *and* perpendicularly to the magnetic field. This in contrast to models with a single ALP, where the amplitude for the parallel (perpendicular) polarization vanishes for a pseudo-scalar (scalar) ALP.

The gray shaded band in the plots indicate a parameter region for the experimental setup where the signals have an oscillatory behavior, corresponding to $|K^{\parallel,\perp}| < \ell^{-1}$ and $|\Delta k^{\parallel,\perp}| > \ell^{-1}$ defined in Eq. (5.6). For $|K^{\parallel,\perp}| \gg \ell^{-1}$, the signal becomes constant with $P_{\text{trans}} = \chi^4$, whereas it can increase by up to a factor of 16 in the oscillatory region, cf. Eq. (4.7).

The solid lines in the center and lower panels of Fig. 5 show the rotation and ellipticity of the laser polarization, respectively in comparison with a pure MCP model (red dashed

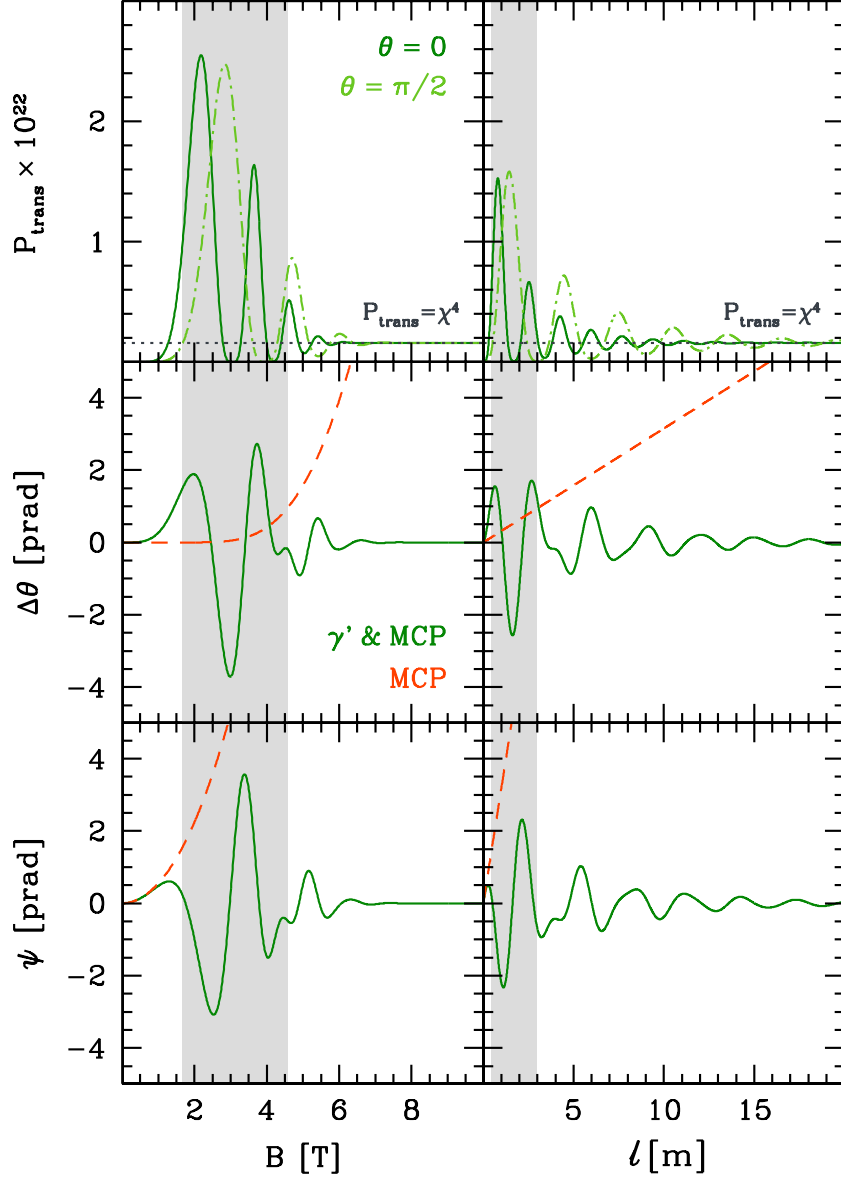


Figure 5: Dependence of the regeneration probability P_{trans} (upper panels), rotation $\Delta\theta$ (center panels), and ellipticity ψ (lower panels) on the magnetic field B (left panels) and the length ℓ of the magnetic region inside the cavity (right panels). As a benchmark point we assume one massless paraphoton with kinetic mixing parameter $\chi = 2 \times 10^{-6}$ and para-coupling $e_h = e$ with a hidden Dirac spinor with mass $m_\epsilon = 0.1$ eV. The remaining experimental parameters are kept at $B = 5$ T, $\omega = 1$ eV, $N_{\text{pass}} = 1$, and $\ell = 5$ m in each plot. The photon regeneration probability is shown for the case of parallel $\theta = 0$ (solid line) and orthogonal $\theta = \pi/2$ (dot-dashed line) laser polarization. The dotted line indicates the asymptotic behavior $P_{\text{trans}} = \chi^4$. The rotation and ellipticity signals assume a polarization of $\theta = \pi/4$. For comparison, the dashed line shows the result for rotation and ellipticity without massless paraphotons (see Ref. [6, 29]). The gray shaded band in each plot indicates the oscillation regime, corresponding to $|K^{\parallel,\perp}| < \ell^{-1}$ and $|\Delta k^{\parallel,\perp}| > \ell^{-1}$ (compare Eqs. (5.6)–(5.8)).

lines). In general, the presence of the paraphoton alters the signals significantly compared to a pure MCP model. In particular, the seemingly favorable experimental parameters, long and strong magnetic fields, lead to a small signal. Only inside the oscillatory region the signals may become comparable to or even larger than the pure MCP signal, as can be seen from the rotation plots.

Note that these qualitative features are generic to the paraphoton model, whereas the specific position of the signal peaks depends on the particular *benchmark* point that is used in the plots. This becomes apparent in Figs. 6 and 7, where now the model parameters are varied while keeping the experimental ones fixed. Again, one finds a similar behavior of the signals on the kinetic mixing parameter χ , the relative para-coupling e_h/e , the mass of the minicharged particle m_ϵ and the mass of the paraphoton μ . For masses of the order of a few $\times 10 \mu\text{eV}$, the most important effect is the reduction of the effective magnetic field as discussed in Sect. 6, since masses in the μeV range are not big enough to lead to a sizeable transition probability from oscillations due to the mass alone. For bigger masses $\gtrsim \text{meV}$, the photon-paraphoton oscillations are driven by the mass term. In this region, the signal does not change if the magnetic field is switched off.

The reason for the fact that ellipticity and rotation become insensitive to the model parameters for large magnetic field length or strength can easily be understood heuristically: owing to the nonzero depletion coefficient κ for the photon interaction state, the combined photon-paraphoton state evolves nonunitarily over long distances into that mixed state which does not interact with the hidden fermions h . For this state, the effective refractive index and depletion coefficient approach the trivial vacuum values; consequently, any further ellipticity or rotation effects are absent in this regime.

It is interesting to observe that the ellipticities in the paraphoton model deviate from the pure MCP model towards smaller values in the oscillatory region, whereas the rotations also exhibit peaks that exceed the pure MCP value, see, *e.g.*, Figs. 5 and 6. The reason for these pronounced rotation peaks in the paraphoton model lies in a nontrivial interplay between the paraphoton and the minicharged fluctuations, as is visible from the second term in Eq. (5.7). In pure MCP models, rotation is induced by photon loss due to MCP production (first term in Eq. (5.7)) for which mass-threshold and phase-space conditions have to be satisfied. With a light paraphoton, these conditions are much more relaxed; for instance, a photon-paraphoton transition via a virtual intermediate MCP state can be possible even if the photon energy is too small to excite a real MCP pair. This rotation-inducing effect is a genuine feature of models with both MCPs and paraphotons. The model-parameter range where these rotation peaks appear is also a promising candidate for parameterizing the anomalous PVLAS rotation signal [2]; a precise fit to the corresponding allowed parameter range, however, is beyond the scope of the present work.

The BFRT collaboration [1, 8] performed a pioneering experiment searching for the rotation, ellipticity, and photon regeneration signals. From the non-observation of a signal one can infer exclusion regions for the MCP scenario as well as extensions with paraphotons. The left plot of Fig. 8 shows the excluded region of mass m_ϵ and charge ϵ

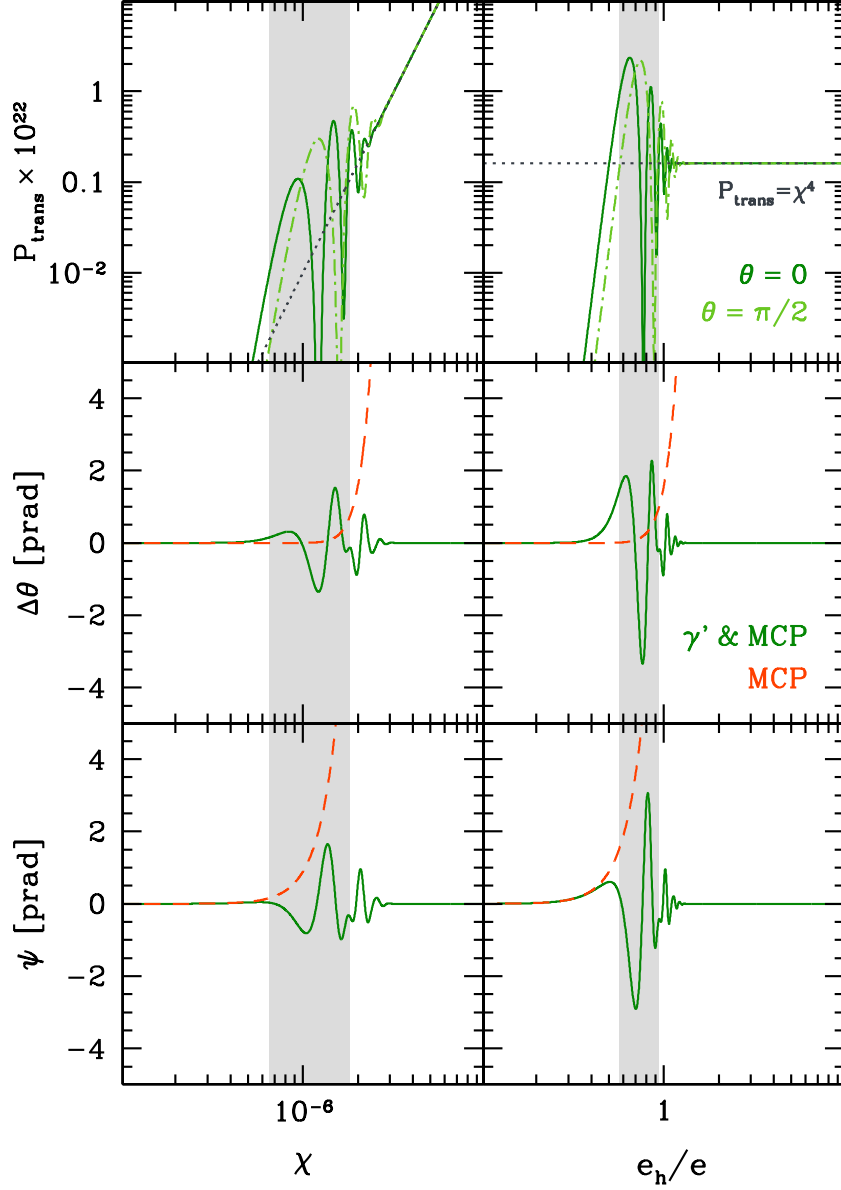


Figure 6: Dependence of the regeneration probability P_{trans} (upper panels), rotation $\Delta\theta$ (center panels), and ellipticity ψ (lower panels) on the kinetic mixing parameter χ (left panels), and the relative para-coupling e_h/e (right panels). We use the same benchmark values and notation as in Fig. 5.

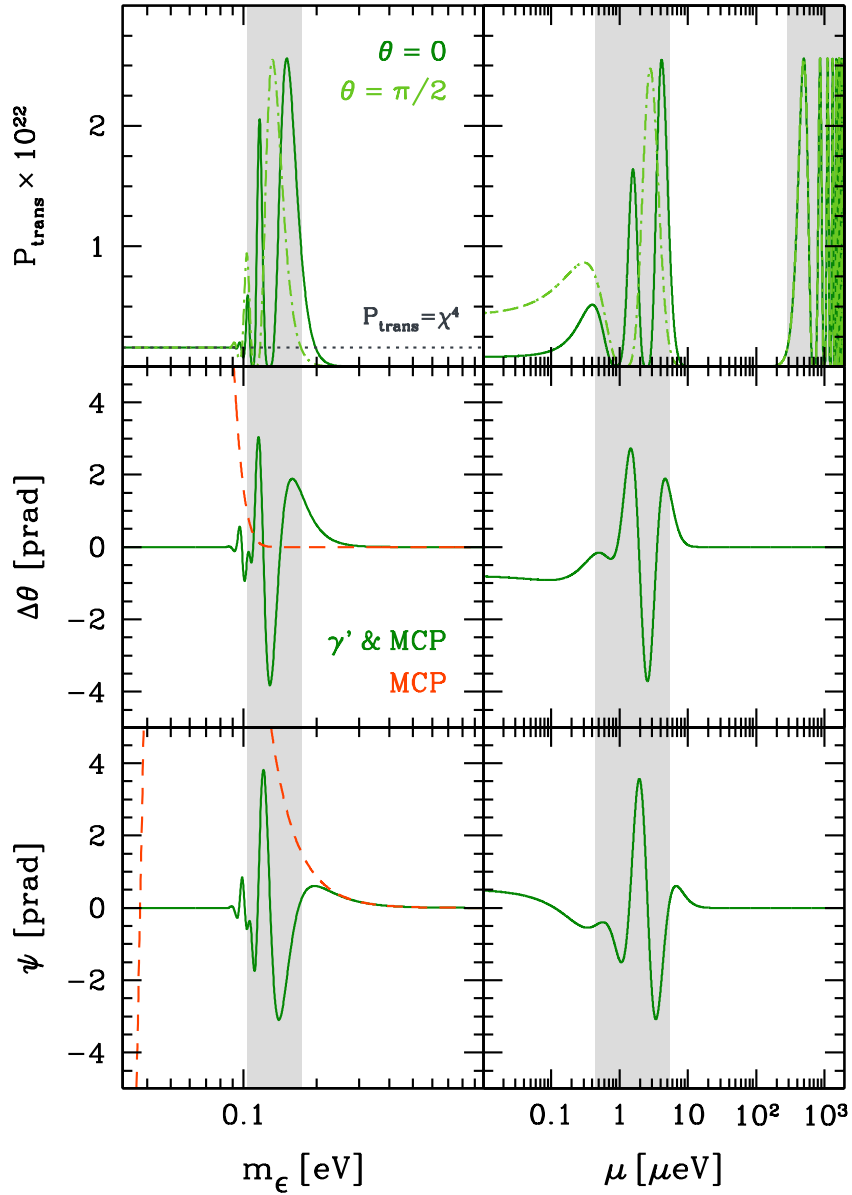


Figure 7: Dependence of the regeneration probability P_{trans} (upper panels), rotation $\Delta\theta$ (center panels), and ellipticity ψ (lower panels) on the mass of the minicharged particle m_ϵ (left panel) and the mass of the paraphoton μ (right panels). We use the same benchmark values and notation as in Fig. 5. In order to calculate the μ dependence, we have assumed a typical distance of the laser beam from the source of the magnetic field of $r = 4$ cm.

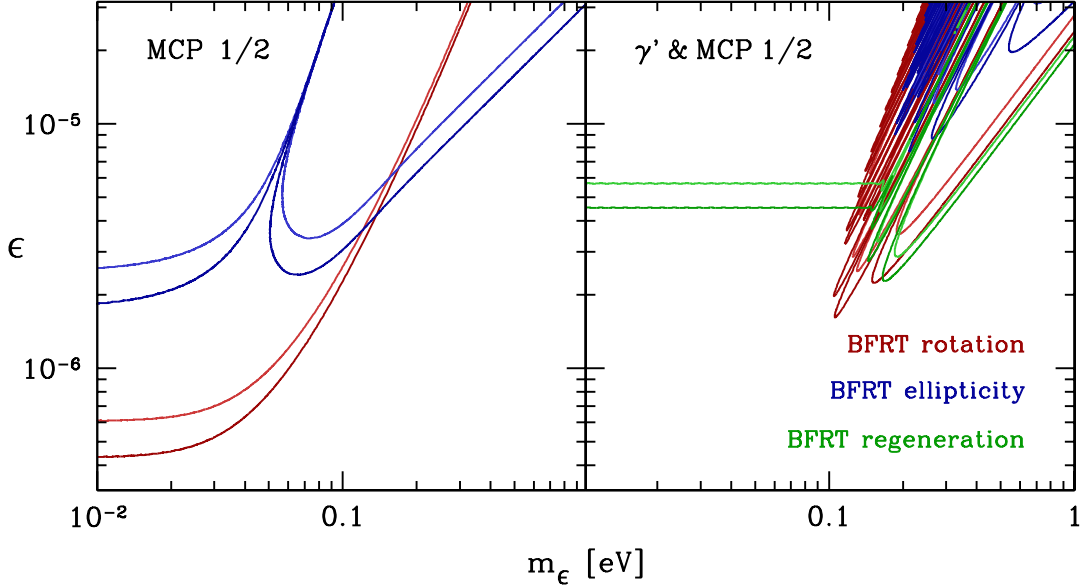


Figure 8: Exclusion limits from the BFRT experiment. The dark (light) contours show the 2σ (5σ) exclusion limits of charge ϵ and mass m_ϵ of a Dirac spinor corresponding to the measurements of the BFRT collaboration. (For simplicity, we assume a constant magnetic field amplitude of $B = 2$ T for the calculation of the rotation and ellipticity signal.) The left panel shows the excluded region in the pure MCP model. The right panel shows the results including a massless paraphoton with para-coupling $e_h = e$. The loss of sensitivity for small masses is partially compensated by the results of the photon regeneration experiment.

in the pure MCP model. In this case, the model is not constrained by the regeneration measurement.

This is different for paraphoton models, as can be seen in the right plot of the same figure. For small masses, rotation and ellipticity do not represent sensitive probes of the model parameter space. However, the regeneration limit puts a constant upper bound on the charge ϵ at small masses m_ϵ and not too small e_h , corresponding to the asymptotic behavior of the transition probability $P_{\text{trans}} \rightarrow \chi^4$. This partially compensates for the loss of sensitivity of the optical measurements. This demonstrates that LSW experiments are complementary to polarization measurements.

Of course, the results are also somewhat dependent on the gauge coupling of the paraphoton, e_h . But, as can be seen from Fig. 9, even a variation of the gauge coupling by one order of magnitude around the natural value e leads to relatively small changes in the limit on χ obtainable from the BFRT regeneration data. This is a significant advantage of LSW experiments.

The qualitative dependence of the limits from LSW measurements on the remaining model parameter, the paraphoton mass μ , can already be inferred from the right upper-most panel in Fig. 7. If we assume a typical distance of the laser beam from the source

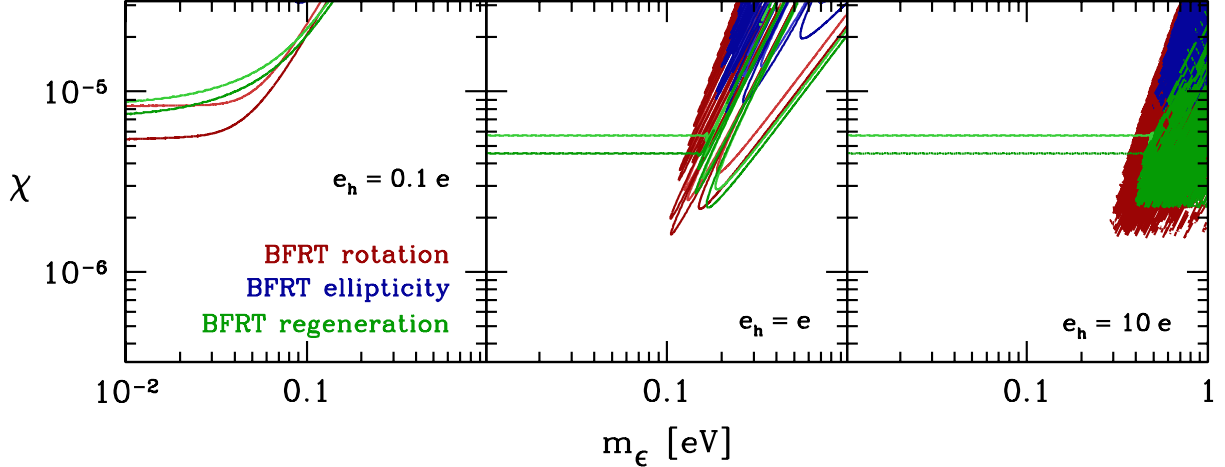


Figure 9: The limit from BFRT measurements on the kinetic mixing parameter for various values of the para-coupling e_h . The 2σ (5σ) exclusion limits are plotted as dark (light) contours.

of the magnetic field of the order of 5 cm, photon regeneration is sensitive in the range $\mu \lesssim 10 \mu\text{eV}$ to oscillations induced by the magnetic field. For bigger masses, this effect is extremely suppressed because the magnetic field is effectively zero, as can be seen from Eq. (6.7). The signal is then driven by oscillations via the mass term, and the BFRT bounds are as in Fig. 3.

Finally, let us comment on the two-paraphoton model of Ref. [34]. In this model, regeneration again leads to the best bounds, as can be seen from Fig. 10.

8 Conclusions

Constraining the multitudinous possibilities to extend the standard model of particle physics requires powerful laboratory tools that do not only search for new particles at higher and higher masses, but also for weakly coupled hidden sectors with potentially light particles. In this work, we have shown that light-shining-through-walls (LSW) experiments represent one of these desired tools to specifically look for a hidden sector with additional $U(1)$ paraphoton gauge groups – in addition to their discovery potential of axion-like particles (ALP), as conventionally discussed in the literature. This becomes evident from Figs. 3, 8, and 10, in which we present limits obtained from the BFRT LSW experiment.

Owing to their specific dependence on both model as well as experimental parameters (see Figs. 5, 6, and 7), LSW experiments are also ideally suited to distinguish between different models such as those involving ALPs or paraphotons. One important example of a feature that allows to distinguish between ALPs and paraphotons is the dependence on

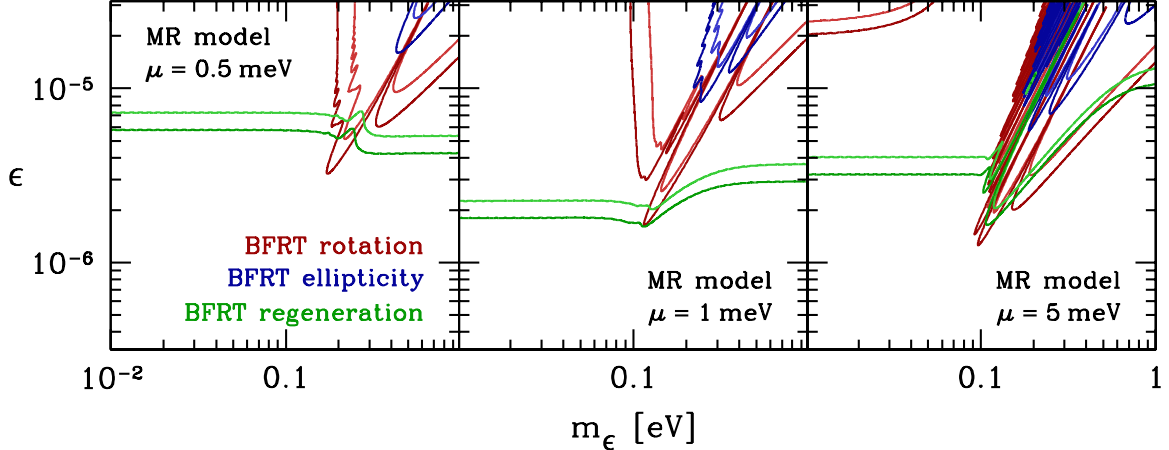


Figure 10: The limit from BFRT measurements on the kinetic mixing parameter in the two-paraphoton model presented in Ref. [34] ($e_h = e$). The 2σ (5σ) exclusion limits are plotted as dark (light) contours. (The chosen values $\mu \sim \text{meV}$ are small enough to avoid the astrophysical constraints and big enough such that effects of the finite size of the magnetic field play no role.)

the polarization of the laser beam. For ALPs, we expect a signal only for one polarization, parallel *or* perpendicular to the magnetic field. In paraphoton models, we expect an LSW signal for *both* polarizations. Also, the dependence of the regeneration rates on experimental parameters such as the laser frequency and the magnetic field are different for the different models and thus provide for further decisive distinguishing criteria.

Polarization experiments provide complementary information (cf. Fig. 8). They are especially sensitive to pure minicharged particle models for which no signal is expected in LSW experiments. However, in paraphoton models, their sensitivity is limited.

In conclusion, regenerating (para-)light from the hidden sector allows to test a large class of natural extensions of the standard model.

The discovery potential of optical experiments for features of the hidden sector is certainly not exhausted by our present study. For instance, the use of the rapidly evolving pulsed high-intensity laser systems for this type of fundamental physics challenges needs to be explored much further, see, *e.g.*, [7, 61]. Also, nonlinear collective effects in photon-plasma interactions [62] may serve as an amplifier of signatures of the hidden sector. Finally, experiments with large electric fields, where light minicharged particles could be produced by the Schwinger mechanism, can provide additional insights [63].

Acknowledgements

HG acknowledges support by the DFG under contract Gi 328/1-4 (Emmy-Noether program). JR acknowledges enlightning conversations with Eduard Massó, Jhon Calsamiglia and Javier Virto, as well as support by a contract from the Universidad Autóma de Barcelona, by the CICYT Project FPA2005-05904 and the DURSI Project 2005SGR00916.

A Refractive index for photons in a magnetic field

The loop diagram depicted in Fig. 4(a) gives the contribution of hidden-sector particles to the complex refractive index for photons. The value of this diagram is well known [64]. Let us define

$$\epsilon^2 e^2 \Delta N = \epsilon^2 e^2 \left(\Delta n + \frac{1}{2\omega} i\kappa \right) = n - 1. \quad (\text{A.1})$$

The contribution from intermediate Dirac spinors (“Dsp”) and scalars (“sc”) with an effective coupling ϵe to photons is given as

$$\Delta n_{\parallel, \perp}^{\text{Dsp/sc}}(\epsilon e \mathbf{B}, m_\epsilon) = -\frac{1}{16\pi^2} \left(\frac{\epsilon e \mathbf{B}}{m_\epsilon^2} \right)^2 I_{\parallel, \perp}^{\text{Dsp/sc}}(\lambda), \quad (\text{A.2})$$

with

$$\begin{aligned} I_{\parallel, \perp}^{\text{Dsp}}(\lambda) &= 2^{\frac{1}{3}} \left(\frac{3}{\lambda} \right)^{\frac{4}{3}} \int_0^1 dv \frac{\left[\left(1 - \frac{v^2}{3} \right)_{\parallel}, \left(\frac{1}{2} + \frac{v^2}{6} \right)_{\perp} \right]}{(1-v^2)^{\frac{1}{3}}} \times \tilde{e}'_0 \left[-\left(\frac{6}{\lambda} \frac{1}{1-v^2} \right)^{\frac{2}{3}} \right] \\ &= \begin{cases} -\frac{1}{45} [(14)_{\parallel}, (8)_{\perp}], & \text{for } \lambda \ll 1, \\ \frac{9}{7} \frac{\pi^{\frac{1}{2}} 2^{\frac{1}{3}} (\Gamma(\frac{2}{3}))^2}{\Gamma(\frac{1}{6})} \lambda^{-4/3} [(3)_{\parallel}, (2)_{\perp}], & \text{for } \lambda \gg 1. \end{cases} \end{aligned} \quad (\text{A.3})$$

and

$$\begin{aligned} I_{\parallel, \perp}^{\text{sc}}(\lambda) &= \frac{2^{\frac{1}{3}}}{2} \left(\frac{3}{\lambda} \right)^{\frac{4}{3}} \int_0^1 dv \frac{\left[\left(\frac{v^2}{3} \right)_{\parallel}, \left(\frac{1}{2} - \frac{v^2}{6} \right)_{\perp} \right]}{(1-v^2)^{\frac{1}{3}}} \times \tilde{e}'_0 \left[-\left(\frac{6}{\lambda} \frac{1}{1-v^2} \right)^{\frac{2}{3}} \right] \\ &= \begin{cases} -\frac{1}{90} [(1)_{\parallel}, (7)_{\perp}], & \text{for } \lambda \ll 1, \\ \frac{9}{14} \frac{\pi^{\frac{1}{2}} 2^{\frac{1}{3}} (\Gamma(\frac{2}{3}))^2}{\Gamma(\frac{1}{6})} \lambda^{-4/3} [(\frac{1}{2})_{\parallel}, (\frac{3}{2})_{\perp}], & \text{for } \lambda \gg 1. \end{cases} \end{aligned} \quad (\text{A.4})$$

Here, the dimensionless parameter λ is defined as

$$\lambda \equiv \frac{3}{2} \frac{\omega}{m_\epsilon} \frac{\epsilon e \mathbf{B}}{m_\epsilon^2} = 88.6 \epsilon \frac{\omega}{m_\epsilon} \left(\frac{\text{eV}}{m_\epsilon} \right)^2 \left(\frac{\mathbf{B}}{\text{T}} \right). \quad (\text{A.5})$$

The symbol \tilde{e}_0 denotes the generalized Airy function,

$$\tilde{e}_0(t) = \int_0^\infty dx \sin\left(tx - \frac{x^3}{3}\right), \quad (\text{A.6})$$

and $\tilde{e}'_0(t) = d\tilde{e}_0(t)/dt$.

Similarly,

$$\kappa_{\parallel,\perp}^{\text{Dsp}}(\epsilon e\mathbf{B}, m_\epsilon)\ell = \frac{1}{2}\epsilon \frac{e}{4\pi} \frac{\mathbf{B}\ell}{m_\epsilon} T_{\parallel,\perp}^{\text{Dsp}}(\lambda), \quad (\text{A.7})$$

$T_{\parallel,\perp}(\lambda)$ has the form of a parametric integral [65],

$$\begin{aligned} T_{\parallel,\perp}^{\text{Dsp}} &= \frac{4\sqrt{3}}{\pi\lambda} \int_0^1 dv K_{2/3}\left(\frac{4}{\lambda} \frac{1}{1-v^2}\right) \times \frac{\left[\left(1 - \frac{1}{3}v^2\right)_\parallel, \left(\frac{1}{2} + \frac{1}{6}v^2\right)_\perp\right]}{(1-v^2)} \\ &= \begin{cases} \sqrt{\frac{3}{2}} e^{-4/\lambda} \left[\left(\frac{1}{2}\right)_\parallel, \left(\frac{1}{4}\right)_\perp\right], & \text{for } \lambda \ll 1, \\ \frac{2\pi}{\Gamma(\frac{1}{6})\Gamma(\frac{13}{6})} \lambda^{-1/3} \left[(1)_\parallel, \left(\frac{2}{3}\right)_\perp\right], & \text{for } \lambda \gg 1, \end{cases} \end{aligned} \quad (\text{A.8})$$

and

$$\begin{aligned} T_{\parallel,\perp}^{\text{sc}} &= \frac{2\sqrt{3}}{\pi\lambda} \int_0^1 dv K_{2/3}\left(\frac{4}{\lambda} \frac{1}{1-v^2}\right) \times \frac{\left[\left(\frac{1}{3}v^2\right)_\parallel, \left(\frac{1}{2} - \frac{1}{6}v^2\right)_\perp\right]}{(1-v^2)} \\ &= \begin{cases} \frac{1}{2} \sqrt{\frac{3}{2}} e^{-4/\lambda} \left[(0)_\parallel, \left(\frac{1}{4}\right)_\perp\right], & \text{for } \lambda \ll 1, \\ \frac{\pi}{\Gamma(\frac{1}{6})\Gamma(\frac{13}{6})} \lambda^{-1/3} \left[\left(\frac{1}{6}\right)_\parallel, \left(\frac{1}{2}\right)_\perp\right], & \text{for } \lambda \gg 1. \end{cases} \end{aligned} \quad (\text{A.9})$$

These expressions have been derived to leading order in an expansion for high frequency [66, 67, 57, 68, 69, 58],

$$\frac{\omega}{2m_\epsilon} \gg 1, \quad (\text{A.10})$$

and for a high number of allowed Landau levels of the minicharged particles [70],

$$\begin{aligned} \Delta N_p &= \frac{\Delta N_{\text{Landau}}}{2} = \frac{1}{12} \left(\frac{\omega^2}{\epsilon e\mathbf{B}}\right)^2 \left(\frac{\Delta\omega}{\omega} + \frac{\Delta\mathbf{B}}{2\mathbf{B}}\right) \gg 1 \\ &\Leftrightarrow \epsilon \ll 4.9 \times 10^{-3} \left(\frac{\omega}{\text{eV}}\right)^2 \left(\frac{\mathbf{T}}{\mathbf{B}}\right) \left(\frac{\Delta\omega}{\omega} + \frac{\Delta\mathbf{B}}{2\mathbf{B}}\right)^{\frac{1}{2}}. \end{aligned} \quad (\text{A.11})$$

In realistic experiments, the variation $\Delta\omega/\omega$ is typically small compared to $\Delta\mathbf{B}/\mathbf{B} \gtrsim 10^{-4}$.

B Preparation of the initial state and cavity effects

Let us devote a few thoughts to the preparation of the initial state. In Sects. 3 and 4, we always started with a pure photon interaction state, $(A, B) = (1, 0)$ or $(A, B_1, B_2) = (1, 0, 0)$. Is this the correct state for a realistic experiment? Naively, the answer is yes, because the light is produced by ordinary matter which interacts only with the photon interaction eigenstate. Still, one might wonder whether the laser apparatus might be so precise that it can prepare eigenstates of the energy and the momentum simultaneously.

Figure 11 shows why this is not really relevant for the case of a typical setup where the laser beam is coupled into the oscillation region via a mirror (we believe that in most experiments such a redirection of the beam is employed at some stage of the experiment; in BFRT as well as PVLAS this is indeed the case). It is simply the mirror that again selects the interaction state and directs only the photon interaction state into the right direction towards the oscillation region. The paraphoton interaction state simply passes through the mirror and is lost.

The bottom line is that the last mirror that couples the beam into the oscillation region selects a pure photon interaction state, and this determines the initial condition.

Next, we address the question as to whether some optical elements as, *e.g.*, a Fabry-Perot cavity with a high finesse could again select a momentum eigenstate. If so, such a state would have a well-defined wavelength and would therefore correspond to a propagation eigenstate – destroying possible oscillations.

In ordinary optics, the transmission coefficient for a Fabry-Perot cavity is

$$T_{\text{FP}} = \frac{T^2}{1 + R^2 - 2R \cos(\delta)}, \quad (\text{B.1})$$

with

$$\delta = 2k\ell \cos(\theta). \quad (\text{B.2})$$

Here, R and T are the transmission and reflection coefficients of the mirrors. We assume no absorption, *i.e.* $T = 1 - R$. The transmission is strongly peaked around $\delta = 0$ and effectively filters out a very narrow wavelength interval of width

$$\frac{\delta\lambda}{\lambda} = \frac{\lambda}{2\mathcal{F}\ell \cos(\theta)}, \quad (\text{B.3})$$

where ℓ is the length of the cavity, and

$$\mathcal{F} = \frac{\pi}{2 \arcsin\left(\frac{1-R}{2\sqrt{R}}\right)} \approx \frac{2\pi}{1-R} \quad (\text{B.4})$$

denotes its finesse; the approximation in the last step holds for $1 - R \ll 1$. θ is the angle of the incident light (cf. Fig. 12) which we will take to be $\theta = 0$ for simplicity.

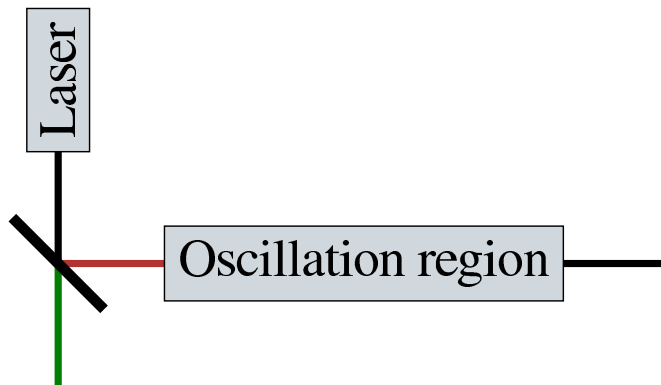


Figure 11: Sketch of the initial-state preparation in a photon-paraphoton oscillation experiment. The laser (including its optical elements) produces some unknown mixture of photon and paraphoton (black line). Now, this beam is redirected via a mirror (black diagonal) into the oscillation region. However, the mirror interacts only with the interaction eigenstate of the photon (red). The paraphoton interaction state simply passes through the mirror (green). Therefore, we have a pure photon interaction state at the beginning of the oscillation region. If the photon interaction state does not coincide with the propagation eigenstates, *i.e.*, if we have mixing, we have a mixed interaction state (black) at the end of the oscillation region.

We can now study what happens in a model with a paraphoton. We start with a pure photon interaction state $(A, B) = (1, 0)$ at the entrance to the cavity. Using the propagation eigenstates found in Sect. 3, we find the amplitude after the first pass through the cavity,

$$T_1 = \begin{pmatrix} A_1 \\ B_1 \end{pmatrix} = T \exp(ik\ell) \begin{pmatrix} \frac{1+\chi^2 \exp(-\Delta k\ell)}{1+\chi^2} \\ \frac{\chi(1-\exp(-\Delta k\ell))}{1+\chi^2} \end{pmatrix}. \quad (\text{B.5})$$

Taking into account that only the photons and not the paraxphotons are reflected by the mirrors, we can easily find also the amplitude for the second transmitted beam,

$$T_2 = \begin{pmatrix} A_2 \\ B_2 \end{pmatrix} = T \exp(3ik\ell) R \left(\frac{1 + \chi^2 \exp(-\Delta k\ell)}{1 + \chi^2} \right)^2 \begin{pmatrix} \frac{1+\chi^2 \exp(-\Delta k\ell)}{1+\chi^2} \\ \frac{\chi(1-\exp(-\Delta k\ell))}{1+\chi^2} \end{pmatrix}. \quad (\text{B.6})$$

Resumming $A_{\text{trans}} = A_1 + A_2 + \dots$, we find the total transition coefficient for the Fabry-Perot cavity,

$$\hat{T}_{\text{FP}} = |A_{\text{trans}}|^2 = \frac{|TM|^2}{1 + |M^2 R|^2 - 2|M^2 R| \cos(\delta + \alpha)}, \quad (\text{B.7})$$

where

$$M = \frac{1 + \chi^2 \exp(-\Delta k\ell)}{1 + \chi^2} =: |M| \exp(i\alpha) \quad (\text{B.8})$$

is the photon-to-photon amplitude for one pass through the cavity. For small χ , we find

$$|M| = 1 - 4\chi^2 \sin^2 \left(\frac{\Delta k\ell}{2} \right), \quad \alpha = 2\chi^2 \sin(\Delta k\ell). \quad (\text{B.9})$$

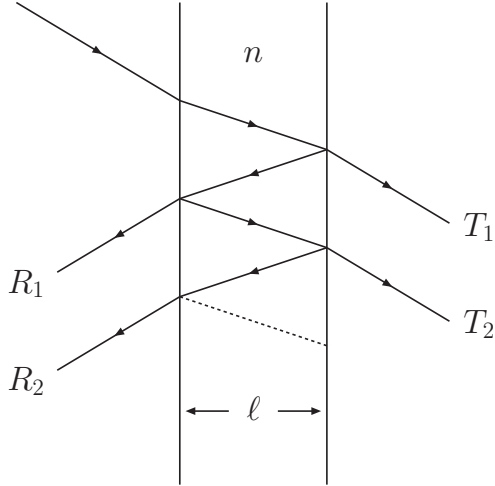


Figure 12: Light path inside a Fabry-Perot cavity.

If $\chi^2 \ll 1/\mathcal{F}$, *i.e.* if more photons escape from the cavity via transmission than via conversion into paraphotons, α and $|M| - 1$ provide only small corrections to the result without paraphotons (B.1), and the cavity selects essentially the same wavelengths around $\delta \approx 2\pi n$ as without paraphotons. For example, in the PVLAS experiment with $\mathcal{F} \sim 10^5$ this condition is easily fulfilled for $\chi \lesssim 10^{-5}$.

Let us now turn to the paraphotons exiting the cavity. The transmission coefficient for paraphotons, or, in other words, the photon-paraphoton conversion probability, is (for small χ),

$$\begin{aligned}
 T_{\text{para}} &= |B_{\text{trans}}|^2 = 4|T|\chi^2 \sin^2\left(\frac{\Delta k \ell}{2}\right) \frac{1}{1 + |M^2 R|^2 - 2|M^2 R| \cos(\delta + \alpha)} \quad (\text{B.10}) \\
 &\approx \frac{2\mathcal{F}}{\pi} \chi^2 \sin^2\left(\frac{\Delta k \ell}{2}\right) \\
 &\approx \frac{N_{\text{pass}} + 1}{2} \chi^2 \sin^2\left(\frac{\Delta k \ell}{2}\right).
 \end{aligned}$$

The last two lines hold for $\chi^2 \ll 1/\mathcal{F}$ and $\delta \approx 2\pi n$, *i.e.*, for incident photons in resonance with the cavity.

To summarize, as long as paraphotons are a “small” effect we rediscover the naively expected result.

C Regeneration probability for the two paraxial model

In this appendix, we give the explicit formulas for the regeneration probability, rotation and ellipticity in the model of Ref. [34] with two paraxial photons.

With the abbreviation $\sqrt{(e_h^2 \Delta n)^2 + (\mu^2/4\omega^2)^2} = \alpha + i\beta$ and $\Delta n = \Delta n + i\kappa/2\omega$, we define the inverse oscillation and absorption lengths Δ_{\pm} and κ_{\pm} , respectively, as

$$\Delta_{\pm} = \omega e_h^2 \Delta n - \frac{\mu^2}{4\omega} \mp \omega, \quad \alpha \quad \kappa_{\pm} = e_h^2 \kappa \mp 2\omega \beta.$$

The transition probability ($\ell_1 = \ell_2 = \ell$ and $N_{\text{pass}} = 1$) is given by the squared sum of the amplitudes for the transition of the wall through the two different paraxial photons

$$P_{\text{trans}} = |\mathcal{A}_{\gamma \rightarrow \gamma'_1 \rightarrow \gamma} + \mathcal{A}_{\gamma \rightarrow \gamma'_2 \rightarrow \gamma}|^2, \quad (\text{C.1})$$

that can be expressed as

$$P_{\text{trans}} = \frac{\chi^4}{X_0^2 + Y_0^2} \left[(2X_0 + X_+ C_+ + X_- C_- + Y_+ S_+ + Y_- S_-)^2 + \begin{pmatrix} X_i \rightarrow Y_i \\ Y_i \rightarrow -X_i \end{pmatrix} \right]. \quad (\text{C.2})$$

Here, the index i denotes $i = (+, -, 0)$, and we have used the functions

$$S_{\pm}(\ell) = \exp(-\kappa_{\pm}\ell) \sin(2\Delta_{\pm}\ell) - 2 \exp(-\kappa_{\pm}\ell/2) \sin(\Delta_{\pm}\ell), \\ C_{\pm}(\ell) = \exp(-\kappa_{\pm}\ell) \cos(2\Delta_{\pm}\ell) - 2 \exp(-\kappa_{\pm}\ell/2) \cos(\Delta_{\pm}\ell),$$

with coefficients

$$X_{\pm} = 16 \left(2e_h^2 \Delta n \frac{e_h^2 \kappa}{2\omega} \pm \beta e_h^2 \Delta n \pm \alpha \frac{e_h^2 \kappa}{2\omega} \right), \quad (\text{C.3}) \\ Y_{\pm} = \frac{\mu^4}{\omega^4} + 16e_h^2 \Delta n (e_h^2 \Delta n \pm \alpha) - 16 \frac{e_h^2 \kappa}{2\omega} \left(\frac{e_h^2 \kappa}{2\omega} \pm \beta \right), \\ X_0 = 32 e_h^2 \Delta n \frac{e_h^2 \kappa}{2\omega}, \\ Y_0 = \frac{\mu^4}{\omega^4} + 16 \left((e_h^2 \Delta n)^2 - \left(\frac{e_h^2 \kappa}{2\omega} \right)^2 \right).$$

The case $B = 0$ corresponds to $\Delta n = \kappa = 0$, giving $\alpha = \frac{\mu^2}{4\omega^2}$ and $\beta = 0$, as well as $\kappa_{\pm} = \Delta_{\pm} = 0$ and $\Delta_+ = -\frac{\mu^2}{2\omega}$. It is straightforward to check that in this case Eq. (C.2) reduces to our previous result Eq. (3.7) with $N_{\text{pass}} = 1$ and $\ell_1 = \ell_2$.

For the photon to photon amplitude we find,

$$\text{Re}(A_{\gamma \rightarrow \gamma}) = 1 - 2\chi^2 + \frac{\chi^2}{\alpha^2 + \beta^2} \quad (\text{C.4})$$

$$\times \left[Z_+ \cos(\Delta_+ \ell) \exp(-\kappa_+ \ell/2) + (+ \rightarrow -) + Z_0 \sin(\Delta_+ \ell) \exp(-\kappa_+ \ell/2) - (+ \rightarrow -) \right]$$

and

$$\begin{aligned} \text{Im}(A_{\gamma \rightarrow \gamma}) &= \frac{\chi^2}{\alpha^2 + \beta^2} \\ &\times \left[Z_+ \sin(\Delta_+ \ell) \exp(-\kappa_+ \ell/2) + (+ \rightarrow -) + Z_0 \cos(\Delta_- \ell) \exp(-\kappa_- \ell/2) - (- \rightarrow +) \right], \end{aligned} \quad (\text{C.5})$$

where

$$\begin{aligned} Z_{\pm} &= \alpha \left(\alpha \pm e_h^2 \Delta n \right) + \beta \left(\beta \pm \frac{e_h^2 \kappa}{2\omega} \right), \\ Z_0 &= \beta e_h^2 \Delta n - \alpha \frac{e_h^2 \kappa}{2\omega}. \end{aligned} \quad (\text{C.6})$$

It is now straightforward to insert this into Eqs. (5.3) and (5.4) to obtain the rotation and ellipticity, respectively.

References

- [1] R. Cameron *et al.* [BFRT Collaboration], Phys. Rev. D **47** (1993) 3707.
- [2] E. Zavattini *et al.* [PVLAS Collaboration], Phys. Rev. Lett. **96** (2006) 110406 [arXiv:hep-ex/0507107].
- [3] S. J. Chen, H. H. Mei and W. T. Ni [Q&A Collaboration], arXiv:hep-ex/0611050.
- [4] L. Maiani, R. Petronzio and E. Zavattini, Phys. Lett. B **175** (1986) 359.
- [5] G. Raffelt and L. Stodolsky, Phys. Rev. D **37** (1988) 1237.
- [6] H. Gies, J. Jaeckel and A. Ringwald, Phys. Rev. Lett. **97** (2006) 140402 [arXiv:hep-ph/0607118].
- [7] T. Heinzl, B. Liesfeld, K. U. Amthor, H. Schworer, R. Sauerbrey and A. Wipf, Opt. Commun. **267**, 318 (2006) [arXiv:hep-ph/0601076].
- [8] G. Ruoso *et al.* [BFRT Collaboration], Z. Phys. C **56** (1992) 505.
- [9] L. B. Okun, Sov. Phys. JETP **56**, 502 (1982).
- [10] P. Sikivie, Phys. Rev. Lett. **51** (1983) 1415 [Erratum-ibid. **52** (1984) 695].
- [11] A. A. Anselm, Yad. Fiz. **42** (1985) 1480.
- [12] M. Gasperini, Phys. Rev. Lett. **59** (1987) 396.
- [13] K. Van Bibber, N. R. Dagdeviren, S. E. Koonin, A. Kerman, and H. N. Nelson, Phys. Rev. Lett. **59**, 759 (1987).

- [14] A. Dupays, C. Rizzo, M. Roncadelli and G. F. Bignami, Phys. Rev. Lett. **95**, 211302 (2005) [arXiv:astro-ph/0510324].
- [15] A. Mirizzi, G. G. Raffelt and P. D. Serpico, arXiv:0704.3044 [astro-ph].
- [16] M. Fairbairn, S. N. Gninenko, N. V. Krasnikov, V. A. Matveev, T. I. Rashba, A. Rubbia and S. Troitsky, arXiv:0706.0108 [hep-ph].
- [17] K. Ehret *et al.* [ALPS collaboration], arXiv:hep-ex/0702023.
- [18] C. Rizzo for the [BMV Collaboration], 2nd ILIAS-CERN-CAST Axion Academic Training 2006, <http://cast.mppmu.mpg.de/>
- [19] GammeV Collaboration, <http://gammev.fnal.gov/>
- [20] K. Baker for the [LIPSS Collaboration], 2nd ILIAS-CERN-CAST Axion Academic Training 2006, <http://cast.mppmu.mpg.de/>
- [21] P. Pugnati *et al.* [OSQAR Collaboration], CERN-SPSC-2006-035, CERN-SPSC-P-331.
- [22] G. Cantatore for the [PVLAS Collaboration], 2nd ILIAS-CERN-CAST Axion Academic Training 2006, <http://cast.mppmu.mpg.de/>
- [23] A. Ringwald, arXiv:hep-ph/0612127.
- [24] R. Battesti *et al.*, arXiv:0705.0615 [hep-ex].
- [25] R. Baier and P. Breitenlohner, Act. Phys. Austriaca **25**, 212 (1967); Nuov. Cim. B **47** 117 (1967).
- [26] S. L. Adler, Annals Phys. **67** (1971) 599.
- [27] S. L. Adler, J. Phys. A **40** (2007) F143 [arXiv:hep-ph/0611267].
- [28] S. Biswas and K. Melnikov, Phys. Rev. D **75** (2007) 053003 [arXiv:hep-ph/0611345].
- [29] M. Ahlers, H. Gies, J. Jaeckel, and A. Ringwald, Phys. Rev. **D75**, 035011 (2007), hep-ph/0612098.
- [30] G. G. Raffelt, Stars As Laboratories For Fundamental Physics: The Astrophysics of Neutrinos, Axions, and other Weakly Interacting Particles, University of Chicago Press, Chicago, 1996.
- [31] S. Davidson, S. Hannestad and G. Raffelt, JHEP **0005** (2000) 003 [arXiv:hep-ph/0001179].
- [32] E. Masso and J. Redondo, JCAP **0509** (2005) 015 [arXiv:hep-ph/0504202].
- [33] P. Jain and S. Mandal, Int. J. Mod. Phys. D **15** (2006) 2095 [arXiv:astro-ph/0512155].

- [34] E. Masso and J. Redondo, Phys. Rev. Lett. **97** (2006) 151802 [arXiv:hep-ph/0606163].
- [35] S. A. Abel, J. Jaeckel, V. V. Khoze and A. Ringwald, arXiv:hep-ph/0608248.
- [36] J. Jaeckel, E. Masso, J. Redondo, A. Ringwald and F. Takahashi, Phys. Rev. D **75** (2007) 013004 [arXiv:hep-ph/0610203].
- [37] R. N. Mohapatra and S. Nasri, Phys. Rev. Lett. **98** (2007) 050402 [arXiv:hep-ph/0610068].
- [38] P. Jain and S. Stokes, arXiv:hep-ph/0611006.
- [39] R. Foot and A. Kobakhidze, Phys. Lett. B **650** (2007) 46 [arXiv:hep-ph/0702125].
- [40] P. Brax, C. van de Bruck and A. C. Davis, arXiv:hep-ph/0703243.
- [41] J. E. Kim, arXiv:0704.3310 [hep-ph].
- [42] A. Melchiorri, A. Polosa and A. Strumia, arXiv:hep-ph/0703144.
- [43] B. Holdom, Phys. Lett. B **166** (1986) 196.
- [44] K. R. Dienes, C. F. Kolda and J. March-Russell, Nucl. Phys. B **492** (1997) 104 [arXiv:hep-ph/9610479].
- [45] D. Lust and S. Stieberger, arXiv:hep-th/0302221.
- [46] S. A. Abel and B. W. Schofield, Nucl. Phys. B **685**, 150 (2004) [hep-th/0311051].
- [47] S. Abel and J. Santiago, J. Phys. G **30**, R83 (2004) [hep-ph/0404237].
- [48] B. Batell and T. Gherghetta, Phys. Rev. D **73** (2006) 045016 [arXiv:hep-ph/0512356].
- [49] R. Blumenhagen, S. Moster and T. Weigand, Nucl. Phys. B **751** (2006) 186 [arXiv:hep-th/0603015].
- [50] S. Davidson, B. Campbell, and D. C. Bailey, Phys. Rev. **D43**, 2314 (1991).
- [51] E. R. Williams, J. E. Faller and H. A. Hill, Phys. Rev. Lett. **26** (1971) 721.
- [52] D. F. Bartlett and S. Loegl, Phys. Rev. Lett. **61** (1988) 2285.
- [53] V. Popov, Turk. J. Phys. **23** (1999) 943.
- [54] F. Wilczek, Phys. Rev. Lett. **40**, 279 (1978).
- [55] S. Weinberg, Phys. Rev. Lett. **40**, 223 (1978).
- [56] J. S. Schwinger, Phys. Rev. **82**, 664 (1951).
- [57] T. Erber, Rev. Mod. Phys. **38**, 626 (1966).

- [58] W. Dittrich and H. Gies, Springer Tracts Mod. Phys. **166**, 1 (2000).
- [59] G. M. Shore, arXiv:hep-th/0701185.
- [60] Y. Liao, (2007), arXiv:0704.1961 [hep-ph].
- [61] A. Di Piazza, K. Z. Hatsagortsyan and C. H. Keitel, Phys. Rev. Lett. **97**, 083603 (2006) [arXiv:hep-ph/0602039].
- [62] M. Marklund and P. K. Shukla, Rev. Mod. Phys. **78**, 591 (2006) [arXiv:hep-ph/0602123].
- [63] H. Gies, J. Jaeckel and A. Ringwald, Europhys. Lett. **76** (2006) 794 [arXiv:hep-ph/0608238].
- [64] W.-y. Tsai and T. Erber, Phys. Rev. **D12**, 1132 (1975).
- [65] W.-y. Tsai and T. Erber, Phys. Rev. **D10**, 492 (1974).
- [66] J. S. Toll, *The Dispersion relation for light and its application to problems involving electron pairs*, PhD thesis, RX-1535.
- [67] N. P. Klepikov, Zh. Eksp. Teor. Fiz. **26** (1954).
- [68] V. Baier and V. Katkov, Zh. Eksp. Teor. Fiz. **53**, 1478 (1967).
- [69] J. J. Klein, Rev. Mod. Phys. **40**, 523 (1968).
- [70] J. K. Daugherty and A. K. Harding, Astrophys. J. **273**, 761 (1983).